Observation of a Photonic Orbital Gauge Field

*Yi-Jun Chang† Chong Sheng† Ying-Yue Yang Yong-Heng Lu Yao Wang Hui-Ming Wang Mingyuan Gao Shi-Bao Wu Hui Liu Shining Zhu Xian-Min Jin**

Yi-Jun Chang, Ying-Yue Yang, Yong-Heng Lu, Yao Wang, Hui-Ming Wang, Shi-Bao Wu
Center for Integrated Quantum Information Technologies (IQIT), School of Physics and Astronomy and State Key Laboratory of Advanced Optical Communication Systems and Networks, Shanghai Jiao Tong University, Shanghai 200240, China
Hefei National Laboratory, Hefei 230088, China
Prof. Chong Sheng, Mingyuan Gao, Prof. Hui Liu, Prof. Shining Zhu
National Laboratory of Solid State Microstructures and School of Physics, Collaborative Innovation Center of Advanced Microstructures, Nanjing University, Nanjing 210093, China
Prof. Xian-Min Jin
Center for Integrated Quantum Information Technologies (IQIT), School of Physics and Astronomy and State Key Laboratory of Advanced Optical Communication Systems and Networks, Shanghai Jiao Tong University, Shanghai 200240, China
Hefei National Laboratory, Hefei 230088, China
TuringQ Co., Ltd., Shanghai 200240, China
Chip Hub for Integrated Photonics Xplore (CHIPX), Shanghai Jiao Tong University, Wuxi 214000, China Email Address: xianmin.jin@sjtu.edu.cn
Yi-Jun Chang, Prof. Chong Sheng
These two authors contributed equally.

Keywords: *Orbital gauge field, Photonic waveguide chip, Vortex light, Disclination defect*

Gauge field is widely studied in natural and artificial materials. With an effective magnetic field for uncharged particles, many intriguing phenomena have been observed in several systems like photonic Floquet topological insulator. However, previous researches about the gauge field mostly focus on limited dimensions such as the Dirac spinor in graphene materials. Here, we firstly propose and experimentally observe an orbital gauge field based on photonic triangular lattices. Disclination defects with Frank angle $\mathbf{\Omega}$ created on such lattices breaks the original lattice symmetry and generates purely geometric gauge field operating on orbital basis functions. Interestingly, it is found that bound states near zero energy with the orbital angular momentum $l = 2$ are intensively confined at the disclination as gradually expanding $\mathbf{\Omega}$. Moreover, the introduction of a vector potential field breaks the time-reversal symmetry of the orbital gauge field, experimentally manifested by the chiral transmission of light on helical waveguides. The orbital gauge field further suggests fantastic applications of manipulating the vortex light in photonic integrated devices.

1 Introduction

A magnetic field usually brings extraordinary properties of particle behaviors such as quantum Hall effect, in which the quantized Hall conductance arises from Landau levels [1]. The quantum Hall effect is the origin of topological insulators [2], and is extended to fractional quantum Hall states which have been proven to realize topological quantum computation [3, 4]. However, the realization of topological insulators is closely associated with stringent conditions of magnetic field. In the past years, artificial gauge fields have been widely studied to realize the effective magnetic field [5, 6], which can be realized in numerous physical systems such as solid state graphene materials, cold atoms and artificial photonic crystals [7–11]. Uncharged particles are capable of simulating various magnetic behaviors by artificial gauge fields, which enrich the methods of controlling particles like edge states in Floquet topological insulator and waveguiding via gauge fields [12, 13]. Wherein, artificial gauge fields are constructed in kinds of spatial dimensions, lots of which focus on the Dirac pseudospinors. It will be appealing to build new dimensions to enlarge the diversity of gauge fields.
Very recently, topological defects are used to generate local gauge flux in electronic materials, liquid crystal films and acoustic structures, which shows exotic characteristics associated with many topological regimes [14–19]. The gauge flux induced by disclination and dislocation defects in materials arises from the unitary transformation of the Dirac spinors and is directly interpreted by geometric curvatures or torsion that break the local translational and rotational crystal symmetries [5, 20, 21]. Dislocations act as point and line defects respectively

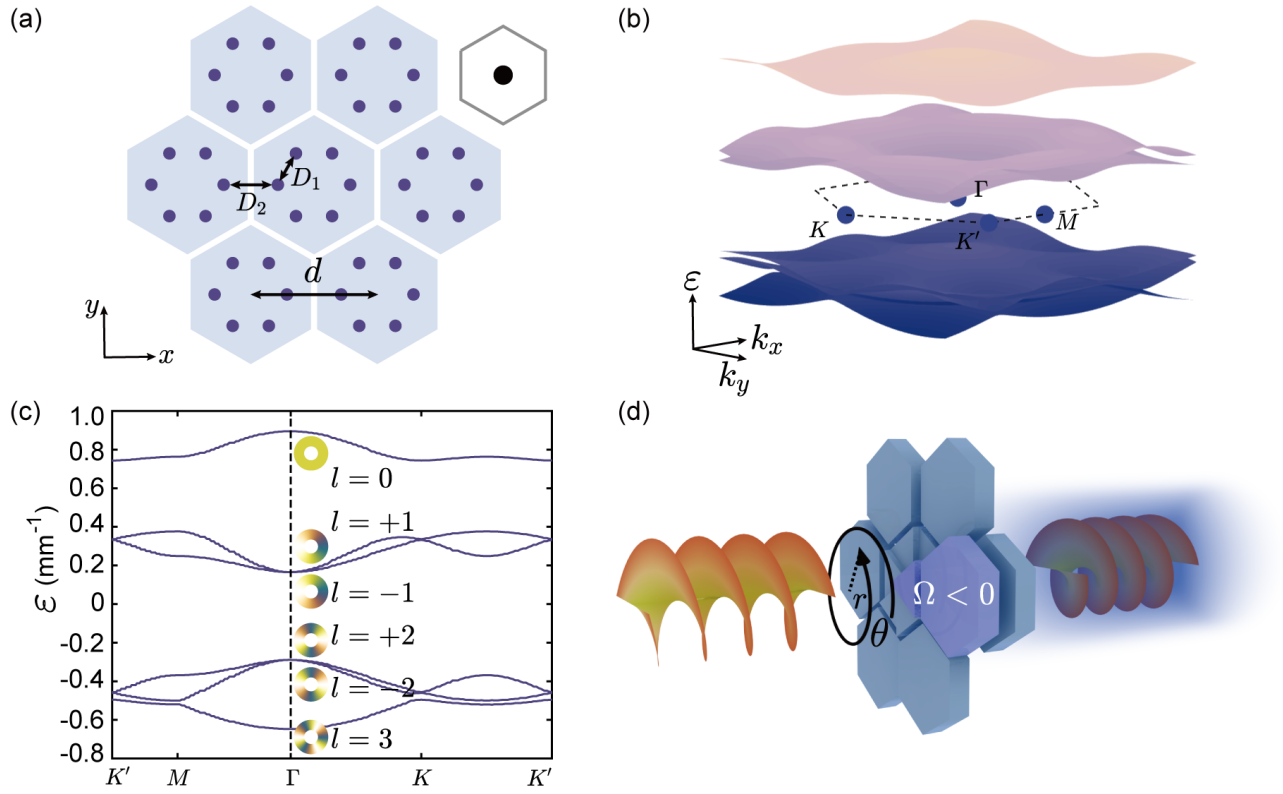

Figure 1: **Photonic triangular lattices and disclination-induced flux.** (**a**) Triangular lattices. D_1 and D_2 represent the spacing distances of intra-cell and inter-cell nearest-neighbor sites, respectively. The inset indicates the Wannier center at the center of a unit cell. (**b**) Energy bands in momentum space of the triangular lattice. (**c**) Energy bands along the highly symmetric points, Γ, K, K', M, as labeled in (b). (**d**) The continuum transformation by inserting a disclination in rotationally symmetric lattices. θ indicates a closed path when inserting extra sections of $\Omega < 0$. The character r indicates the rotational transformation along the uniform circle path.

in two-dimensional and three-dimensional crystalline order, which are represented by a Burger vector [22–24]. Disclinations induce rotational disruption of the crystalline order by a Frank angle [25]. The singular spatial curvature in dislocations and disclinations binds an excess fractional charge respectively acting as dipoles and fractons [26–29], also manifested by bound states at defects linked with topological insulators and non-Euclidean geometries [30–33]. Till now, the local gauge field has always relied on Dirac spinors that has limited dimensions. Due to the rotational symmetry around disclination defects, orbital angular momentum (OAM) of quantum states may create fascinating prospect for new kinds of gauge fields.

The dimension of OAM has been applied in lots of research platforms owing to its infinite scalability. Especially, the optical vortex states are intensively concerned due that the huge spatial dimension of OAM can greatly increase the information capacity in optical communication, imaging and photonic computation [34, 35]. In integrated photonic devices, rotational structures are often designed to generate and transmit vortex states [36–38]. The preserved rotational symmetries at disclinations in topological lattices make it advantageous to confine vortex states [39, 40]. In contrast to the topological insulator dependent on Dirac spinors, a gauge field operating on orbital modes has more powerful capacity of controlling high-dimensional quantum states, which will play a key role in the orbital photonics.

In this letter, we experimentally implement various orbital gauge fields using three kinds of disclinations, which are induced by uniformly rotational deformation to the original triangular lattice through inserting extra pieces of lattices with the six-fold rotational symmetry. As the Frank angle Ω of disclinations expands from 0 to $-\pi/3$ and $-2\pi/3$, the gauge fields operating on orbital bases at the center become stronger and the vortex light carrying OAMs gradually behaves as almost diffractionless transmission near the center of gauge fields. Furthermore, when the orbital gauge field is combined with an effective vector potential, the degenerate vortex modes in gap go through distinct transition and exhibit chiral transport properties. The orbital gauge field demonstrates a novel effective magnetic field and shows remarkable control of particle behaviors in vortex modes.

2 Results

2.1 Theoretical model of the orbital gauge field

The photonic triangular lattices consist of periodic waveguides of unit cells each containing six sites as shown in Fig. 1(a), which possess the six-fold rotational symmetry. The waveguides are fabricated by femtosecond laser direct writing technique, detailed in Methods. The Wannier centers are adapted to the center of each unit cell, as shown in the inset of Fig. 1(a), by choosing the spacing distances between sites in a unit cell $D_1 = 12\,\mu\mathrm{m}$ to be smaller than that between sites in neighboring unit cells $D_2 = 18\,\mu\mathrm{m}$ with the lattice constant $d = 2D_1 + D_2$. The behavior of photons transferring on the photonic lattice obeys an equivalent Schrödinger equation $i\partial_z\Psi = \hat{H}\Psi$, with evolution length z considered as time t. Consequently, in the tight-binding approximation, the Hamiltonian is described by,

$$\hat{H} = \sum_{\langle p,q\rangle}(\kappa_{pq}a_p^\dagger a_q + \mathrm{H.c.}) + \sum_{\langle\langle p,q\rangle\rangle}(\kappa'_{pq}a_p^\dagger a_q + \mathrm{H.c.}), \tag{1}$$

where $a_p^\dagger$ and a_q are creation and annihilation operators acting on single-mode bases in waveguides p and q, respectively, and the couplings of photons transmitting on waveguides only consider κ_{pq} between the nearest-neighbor sites and κ'_{pq} between the next-nearest-neighbor sites in one unit cell.

After transforming the Hamiltonian Eq. (1) into the Fourier momentum space, the energy bands ε in the first Brillouin zone are displayed in Fig. 1(b). Along the highly symmetric points $\Gamma(0,\,0)$, $K(-4\pi/3d, 0)$, $K'(-2\pi/3d,$ $-2\pi/\sqrt{3}d)$, $M(0, -2\pi/\sqrt{3}d)$ labeled by blue dots in Fig. 1(b), the energy bands are more detailed in Fig. 1(c). Due to the unequal couplings κ_1 intra a unit cell and κ_2 inter neighboring unit cells respectively corresponding to spacing distances D_1 and D_2 with an exponentially decreasing relation, a gap is opened at the double Dirac cones near zero energy [41]. At Γ, the Hamiltonian is diagonalized as $\hat{H}_0^{\mathrm{OAM}}$ by similarity transformation and the basis functions are transformed into six vortex modes $|\Psi_l\rangle$, $l = 0, \pm1, \pm2, 3$, as shown in the insets of Fig. 1(c). Based on the same similarity transformation, the Hamiltonian near Γ point in momentum space is approximately described through low-energy effective theory [42], $\hat{H}_\Gamma^{\mathrm{OAM}}(\boldsymbol{\delta}\mathbf{k}) = \hat{H}_0^{\mathrm{OAM}} + v_F(\delta k_x\Sigma_x + \delta k_y\Sigma_y)$, where $v_F = \kappa_2 d$, and Σ_x, Σ_y are commutative operators (see Supplementary Note 1 for details). Different to a spin-Dirac equation that acts on the four-component spinor [30], the atom-like Hamiltonian of the triangular lattice shows higher capacity of Hilbert space in orbital bases that are easily scalable.

The transformed basis functions show rotational symmetry about the center of a unit cell. An extra section inserted in the original triangular lattice induces the rotational deformation that generates a point defect of disclination with $\Omega < 0$, which has negative curvature similarly existing in carbon nanotubes [5]. Considering a continuum transformation description as shown in Fig. 1(d), the rotational deformation due to new sections requires satisfaction of specific boundary conditions for six different orbital basis functions on the lattice as, $\Psi'(r, \theta = 2\pi) = \Psi(r, \theta = 2\pi - \Omega) = e^{-i(2\pi-\Omega)L_6}\Psi'(r, \theta = 0)$, with the diagonal matrix $L_6 = \mathrm{diag}\{0, 1, -1, 2, -2, 3\}$. Correspondingly, the wavefunction will change in the azimuthal phase term, $\Psi'(r, \theta) = e^{i\chi(\theta)}\Psi(r, \theta)$ with $\chi(\theta) = \frac{\Omega}{2\pi}\theta L_6$, which induces a gauge transformation $U = e^{i\chi(\theta)}$ acting on six-component wavefunctions. After the same gauge transformation $U(\theta)\hat{H}_\Gamma^{\mathrm{OAM}}(\boldsymbol{\delta}\mathbf{k})U^\dagger(\theta)$, the Hamiltonian $\hat{H}_\Gamma^{\mathrm{OAM}}(\boldsymbol{\delta}\mathbf{k})$ adds a purely geometric gauge field in lattices [43, 44], $\mathbf{w} = -\nabla\chi = -\Omega L_6/2\pi r \cdot \mathbf{e}_\theta$, operating on orbital basis functions $|\Psi_l\rangle$. Hence, the effective Hamiltonian is transformed as,

$$\tilde{\hat{H}}_\Gamma^{\mathrm{OAM}} = \hat{H}_0^{\mathrm{OAM}} - iv_F\tilde{\boldsymbol{\Sigma}}\cdot[\nabla + i\mathbf{w}], \tag{2}$$

where $\tilde{\boldsymbol{\Sigma}} = \tilde{\Sigma}_x\mathbf{e}_x + \tilde{\Sigma}_y\mathbf{e}_y$ transformed from Σ_x, Σ_y are still commutative operators and $\mathbf{e}_x, \mathbf{e}_y, \mathbf{e}_\theta$ are basis vectors respectively in Cartesian and cylindrical coordinates (see Supplementary Note 1 for detailed analysis of boundary conditions and the gauge transformation).

The gauge field $\mathbf{w}$ is independent on the azimuthal angle θ and is concentrated at the center of disclination. Along a closed curve of θ in Fig. 1(d), an effective flux by integrating the geometric gauge field $\mathbf{w}$ is equal to $-\Omega L_6$, acquired as the phase shift of rotating transformation [43].

As usually discussed before [30, 43], the spinor gauge field generated at the disclination in graphene structures is able to confine mid-gap states. The orbital gauge field operating on photonic vortex modes similarly shifts bulk

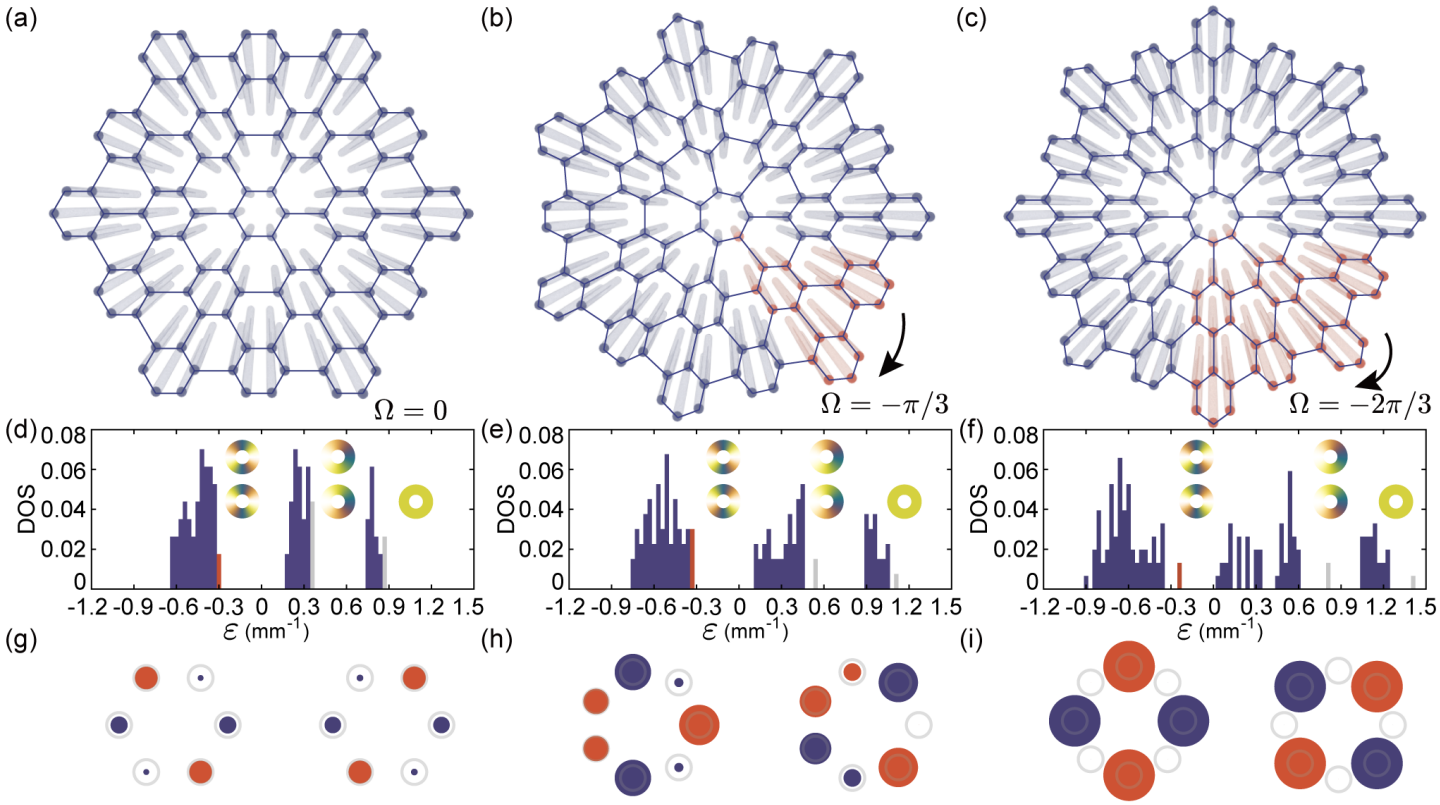

Figure 2: **In-gap states due to the various orbital gauge fields.** (**a-c**) Triangular lattices with no disclination and with disclinations of $\Omega = -\pi/3$ and $-2\pi/3$. The red waveguides indicate the inserted extra sections to original triangular lattices. (**d-f**) Calculated DOS of three triangular lattices. The red and gray columns represent degenerate states in three gaps, and the red ones lie in the zero-energy gap, of which distributions near the center of disclination defects are displayed in (**g-i**). Red and purple dots respectively correspond to 0 and π phase of states, and the size of dots indicates the local density of states at central sites positioned by gray circles.

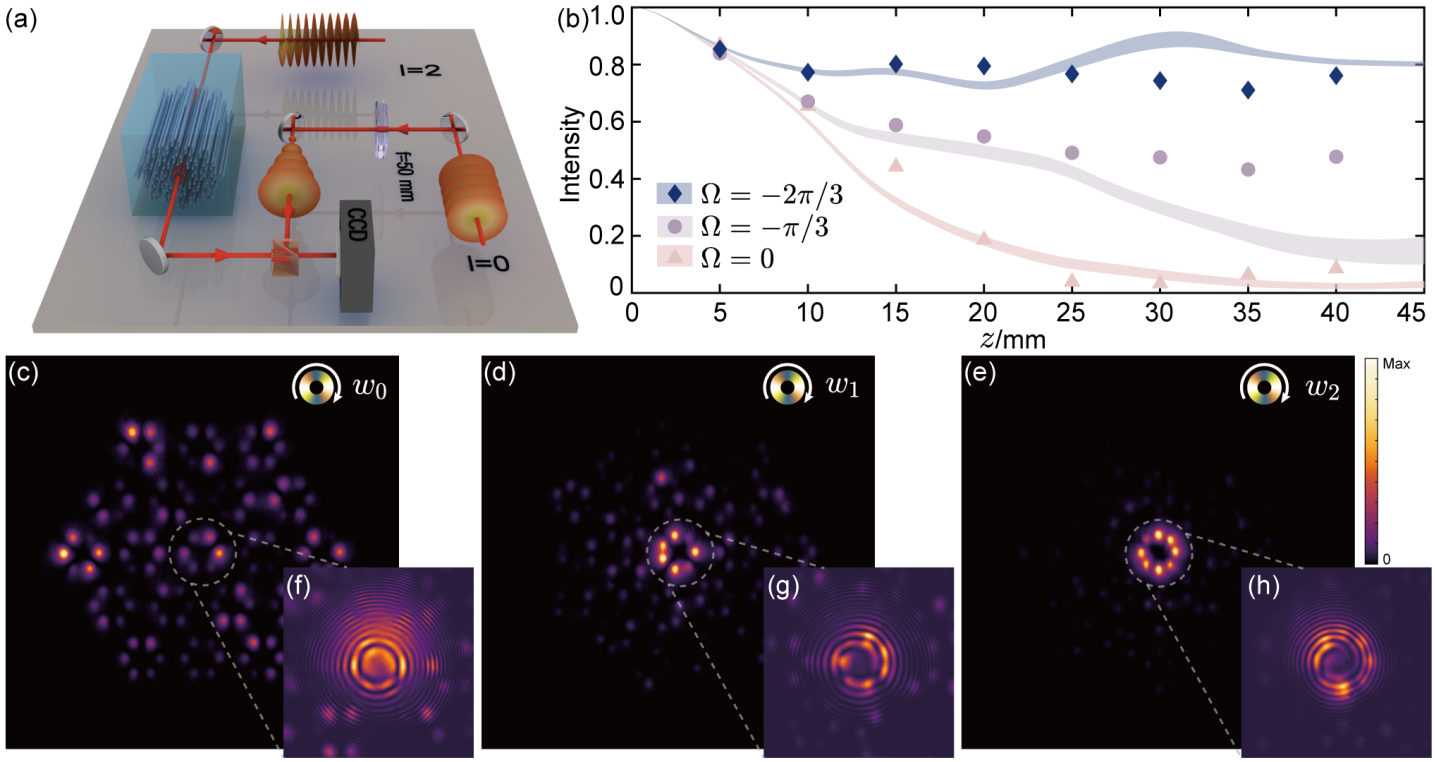

Figure 3: **Experimental propagation of vortex states carrying OAM $l = +2$ as increasing w.** (**a**) Experimental devices. The plane wave light and vortex light come from the same continuous coherent laser, and the latter is produced by a spatial light modulator. The vortex light transmitting on photonic lattices is detected by a CCD, and the plane wave is transformed to a spherical wave by a lens with a focal length of 50 mm to interfere with the vortex state. (**b**) Normalized light intensities at the disclination center for three lattices with evolution length $z = 0$ to 40 mm. Shadow regions and solid marks are respectively simulated and experimental results. The simulated results consider 100 samples with random positional deviations of waveguides $\mathbf{r}_p^{\mathrm{S}} = \mathbf{r}_p \pm (0.25\,\mu\mathrm{m}, 0.25\,\mu\mathrm{m})$. (**c-e**) The intensity distribution for three lattices at $z = 40$ mm. The dashed lines indicate the position for injecting vortex light and interference. (**f-h**) The corresponding interference patterns.

modes into the upper energy gaps. Differently, the orbital gauge field induces bound states in several gaps. Vortex modes in several gaps are able to be separately excited and transmit without diffraction into the bulk materials, which increases the capacity of transmission channel [45]. The triangular lattices with no disclination and with disclinations of $\Omega = -\pi/3$ and $-2\pi/3$ consist of waveguide arrays respectively as shown in Fig. 2(a-c). In contrast to the original triangular lattice with $\mathbf{w}_0 = 0$, creating the disclination of $\Omega = -2\pi/3$ induces larger gauge field $\mathbf{w}_2 = L_6/3r \cdot \mathbf{e}_\theta$ than that $\mathbf{w}_1 = L_6/6r \cdot \mathbf{e}_\theta$ of $\Omega = -\pi/3$. By diagonalizing the Hamiltonians in Eq. (1) of the three lattices, the densities of states (DOS) are obtained in Fig. 2(d-f). As the three gauge fields interact with the effective Hamiltonian in Eq. (2), the bound states carrying OAMs of $l = \pm 2, \pm 1, 0$ gradually arise in corresponding gaps, marked by red and gray columns in Fig. 2(d-f), whereas the vortex mode of $l = 3$ is always surrounded by bulk states (see Supplementary Note 2 for detailed properties of various bound states). The orbital gauge field $\mathbf{w}$ is capable of confining high-dimensional vortex states that are applicable in multimode transport.

Considering the zero-energy gap breaking the doubly degenerate Dirac cones [41], the two degenerate states perform intensely distinguishable density distribution at the center of various disclinations, as shown in Fig. 2(g-i). The central states are exactly the superposition of vortex modes carrying OAM $l = \pm 2$. Obviously, the local density of states at the center of $\mathbf{w}_2$ is stronger than that of $\mathbf{w}_0$ and $\mathbf{w}_1$, which indicates the increasing confinement of vortex modes by expanding orbital gauge fields.

2.2 Experimental demonstration of the orbital gauge field

In experiment, the vortex light produced by a spatial light modulator is focused on the front facet of the waveguide chip [36], as shown in Fig. 3(a). After transmitting on lattices, the output light is detected by a charge-coupled

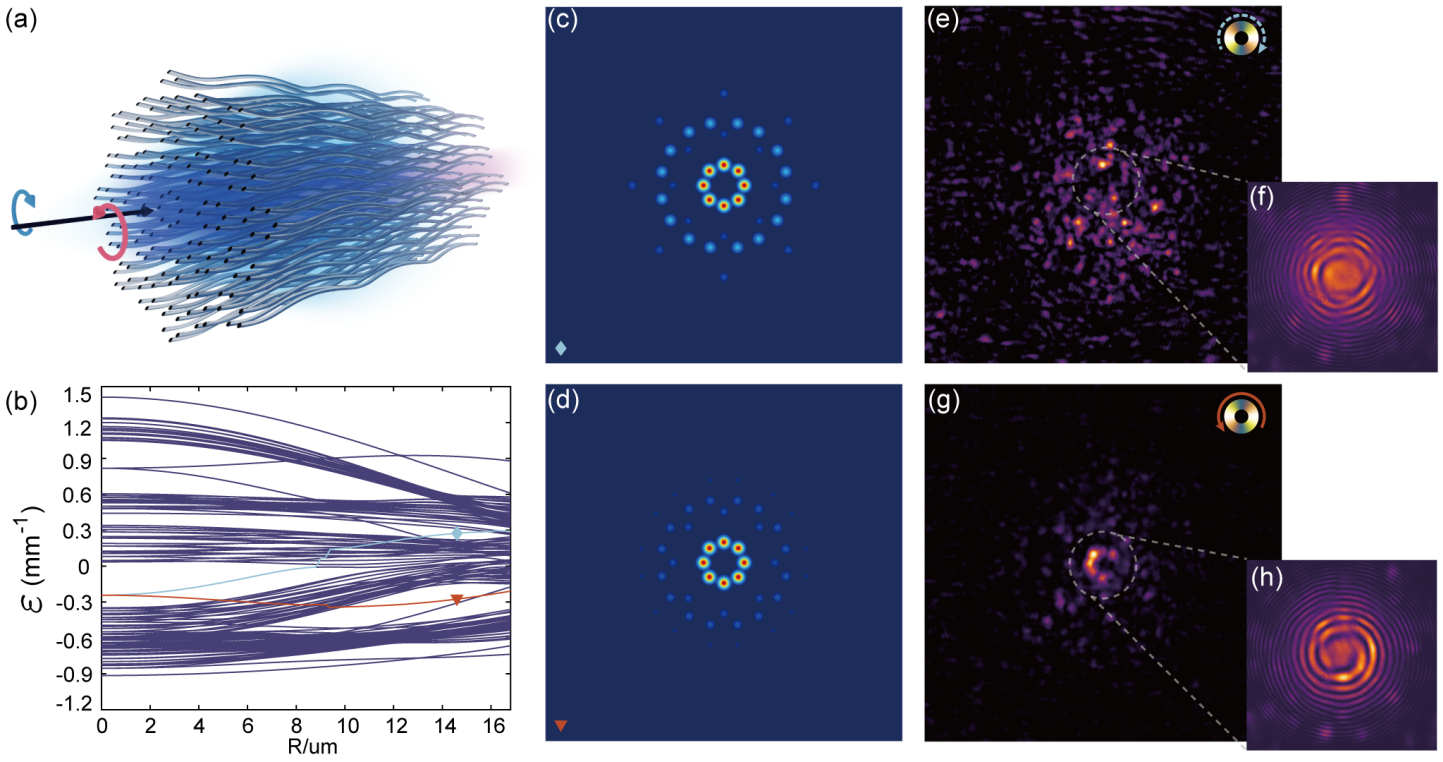

Figure 4: **Symmetry-broken in-gap states.** (**a**) Triangular lattices consisted of helical waveguides. Blue and red circle arrows respectively indicate the vortex light $l = +2$ and $l = -2$ on the lattice. (**b**) Energy bands as the radius of helical waveguides changes. (**c**) The intensity distribution of the eigenmode marked by a blue diamond in (b). (**d**) The eigenmode marked by a red triangle in (b). (**e-f**) The experimental intensity distribution and interference pattern of vortex light $l = +2$ at evolution length $z = 50$ mm. The dashed lines indicate the position for injecting vortex light and interference. (**g-h**) Vortex light $l = -2$.

device (CCD) camera. To analyze the phase characteristic of vortex light, the interference with a spherical wave is performed by adding a beam splitter (BS) before the CCD camera.

The photonic vortex states of $l = +2$ are dynamically transmitted on the triangular lattices with disclinations of $\Omega = 0, -\pi/3$ and $-2\pi/3$. As the evolution length varies from $z = 0$ to 40 mm, normalized mode intensities concentrated at the disclination center are experimentally tested as shown in Fig. 3(b), which are almost consistent with the simulated results represented by shadow regions. The central intensity on the original triangular lattice rapidly decreases to zero. In contrast, the central intensities in the presence of gauge fields $\mathbf{w}_1$ and $\mathbf{w}_2$ tend to stabilize near 0.47 and 0.75, respectively. The gauge field $\mathbf{w}_2$ behaves effectively as a strong magnetic field that confines the vortex modes at the center.

In more detail, the intensity distribution and interference patterns of vortex states at evolution length $z = 40$ mm are displayed in Fig. 3(c-e) and in Fig. 3(f-h), respectively. The vortex states diffuse into bulk lattices with $\mathbf{w}_0$, and hence the phase diagrams are destroyed, indicated by interference patterns as displayed in Fig. 3(f). Obviously, the vortex modes carrying OAM $l = 2$ keep nearly original performance of both intensity and phase characteristics, depicted in Fig. 3(d-e) and Fig. 3(g-h), suggesting that the increasing gauge fields $\mathbf{w}_1$ and $\mathbf{w}_2$ gradually build an ideal channel for transmitting vortex light.

2.3 Interaction with a vector potential field

Furthermore, the time-reversal symmetry of the orbital gauge field is broken, combined with an effective z-dependent vector potential in photonic systems [12], $\mathbf{A}(z) = k_0 RW(\sin Wz, -\cos Wz)$. As shown in Fig. 4(a), the radius R and modulation frequency $W = 2\pi/T$ of helical waveguides with periodicity $T = 8$ mm affect general properties of the z-dependent Hamiltonian, which transforms from Hamiltonian Eq. (1) as,

$$\hat{H}(z) = \sum_{\langle p,q \rangle} (\kappa_{pq} e^{i\mathbf{A}(z)\cdot(\mathbf{r}_q - \mathbf{r}_p)} a_p^\dagger a_q + \text{H.c.}) + \sum_{\langle\langle p,q \rangle\rangle} (\kappa'_{pq} e^{i\mathbf{A}(z)\cdot(\mathbf{r}_q - \mathbf{r}_p)} a_p^\dagger a_q + \text{H.c.}), \tag{3}$$

where $\mathbf{r}_{p\,(q)}$ is the starting coordinate of site $p\,(q)$. The vector potential $\mathbf{A}(z)$ leads to remarkable changes in generating the orbital gauge field in Eq. (2). Due that couplings between next-nearest-neighbor sites can hardly affect the inclination shape of energy bands, detailed in Supplementary Note 3, the low-energy effective equation is only established with nearest-neighbor couplings, in which the orbital gauge field $\mathbf{w}$ arising from the gauge transformation $U = e^{i\chi(\theta)}$ acts as,

$$\tilde{\hat{H}}_{\Gamma}^{\mathrm{OAM}} = \hat{H}_{0}^{\mathrm{Eff\&OAM}} - i(v_{\mathrm{F}}^{0}\tilde{\mathbf{\Sigma}} + v_{\mathrm{F}}^{\prime}\tilde{\mathbf{\Sigma}}^{\boldsymbol{\prime}}) \cdot [\nabla + i\mathbf{w}], \tag{4}$$

where $v_{\mathrm{F}}^{0} = v_{\mathrm{F}} J_0(A_0 b)$ with $A_0 = k_0 RW$ is much closer to zero than $v_{\mathrm{F}}^{\prime}$ that emerges in the vector potential field, detailed in Supplementary Note 3. Different to the orbital gauge field in static Hamiltonians, the degeneracy of OAM states is broken by the vector potential, and $\tilde{\Sigma}_x^{\prime}, \tilde{\Sigma}_y^{\prime}$ are not commutative, pretty similar to spin operators rather than $\tilde{\Sigma}_x, \tilde{\Sigma}_y$ that are commutative.

Concretely, the bound vortex states in three orbital gauge fields perform exotic features with interaction of the vector potential field. The quasienergy bands ε of the z-dependent Hamiltonian Eq. (3) is obtained based on Floquet-Bloch theory [46–48] (see Methods for calculation of quasienergy). The broken time-reversal symmetry of gauge field $\mathbf{w}_2$ leads to inconsistent behaviors of vortex modes with opposite OAMs.

As the amplitude of $\mathbf{A}(z)$ is increased with larger helical radius R, the degenerate states in the gap near zero energy are gradually split, as depicted in Fig. 4(b). At $R = 14.7\,\mu\mathrm{m}$, the vortex mode of $l = +2$ gets close to the bulk energy bands and that of $l = -2$ is still in gap, which is also suggested by the occupied density of states of vortex states (see Supplementary Note 4 for detailed calculation of occupied density of states). Consequently, the latter exhibits intense concentration at disclination center while the former is more easily perturbed by bulk states, consistently suggested by the eigenmodes in Fig. 4(c-d) and the experimental examinations of both the intensity and interference patterns in Fig. 4(e-h). Consequently, vortex modes of $l = +2$ and $l = -2$ perform chirally asymmetric transmission when a vector potential breaks the time-reversal symmetry of the orbital gauge field.

2.4 Statistical analysis

To observe the orbital gauge field in photonic triangular lattices, we totally design four kinds of structures containing triangular lattices with disclinations of $\Omega = 0, -\pi/3$ and $-2\pi/3$, and triangular lattices consisting of helical waveguides with $-2\pi/3$ disclination. The propagation of vortex light on each structure is characterized by samples of different evolution lengths z. The experimental results are statistically analyzed by considering the fabrication fluctuation of waveguide arrays and environmental noises of light intensity detection.

During the fabrication of waveguide arrays, the focus position of femtosecond laser is moved by a highly precise three-axis motion stage, and the position fluctuation is considered in a small random range $\mathbf{r}_p^{\mathrm{S}} = \mathbf{r}_p \pm (0.25\,\mu\mathrm{m}, 0.25\,\mu\mathrm{m})$, where $\mathbf{r}_p$ is the cross-sectional position of the waveguide on site p. To analyze the statistical results of normalized light intensities at the disclination center, we simulate the propagation process one hundred times for triangular lattices with disclinations of $\Omega = 0, \Omega = -\pi/3, \Omega = -2\pi/3$, considering the position fluctuation of waveguides. We show the statistical simulation results of $\overline{\mathrm{Intensity}} \pm \sigma_n$ as the shadow regions in Fig. 3(b), in which $\overline{\mathrm{Intensity}}$ and σ_n are respectively the mean value and standard deviation of randomly statistical results for one hundred simulated samples calculated by the $MATLAB$ software.

To experimentally examine the propagation process of vortex light on the samples of evolution length z, we use the CCD camera to detect the output spot patterns of light and analyze the intensity distribution using the software of $LBP2\,Series$ of Newport Corporation. After that, we recognize the light spots emitted from all samples, as shown in Fig. 3(c-h), and Fig. 4(e-h). To eliminate the influence of environmental noises, we sum up the regions greater than $1/e$ of the maximum light intensity near each spot by considering statistically Gaussian distribution of each spot, where e is a mathematical constant. Using the above calculated values of sites that are normalized to one, we derive the experimental results of normalized light intensities at the disclination center of vortex light.

3 Conclusion

In summary, we have firstly proposed and experimentally implemented the gauge field based on the orbital dimensions, and realized the chiral transmission of the vortex light in photonic waveguide lattices. The orbital gauge field shows higher-dimensional properties than gauge fields dependent on Dirac spinors. The vortex modes carrying OAMs are well confined by the gauge field $\mathbf{w}_2 = L_6/3r \cdot \mathbf{e}_\theta$ and split by an effective vector potential, feasibly controlling the local transport of high-dimensional orbital states and possibly linked with the orbital Hall effect [49]. In photonic systems, the orbital gauge field can be applied in different symmetric structures and exhibits superior manipulation of vortex light than topological regimes of Floquet topological insulator and topological crystalline insulator that have been implemented in acoustic structures, and provides larger capacity of transmission channel in photonic integrated devices. [19, 40] (see Supplementary Note 5, 6, 7 and 8 for detailed analysis).

The orbital gauge field induced by disclinations manifests the flexible control of transferring a vortex state, which suggests applications of the vortex laser, demultiplexer and isolator in optical devices [50–52] and also enriches the dimension of quantum information processing [53]. It is promising to apply the orbital gauge field to implement novel functions in nonlinear and quantum photonic devices [54–56]. The degree of freedom of OAM plays an essential role in quantum mechanics of the atomic physics and constantly stimulates the development in fundamental physical regimes such as the orbital Hall effect [49], which may also suggest the progress in orbital photonics.

4 Theoretical and Experimental Methods

Detailed parameters of the photonic chip:

The photonic chip contains photonic triangular lattices and auxiliary waveguides, which are all fabricated by the femtosecond laser with a repetition rate of 1 MHz on the borosilicate substrate. The central wavelength of femtosecond laser is 513 nm, the pulse duration 290 fs, and pulse energy 190 nJ. To get waveguides with uniform parameters at different depths, the laser beam is shaped by a spatial light modulator and then focused by a 50X objective (numerical aperture 0.55) to write waveguides along specific trajectories. Focus depth of laser is $200\pm100\,\mu$m below the surface for three kinds of triangular lattices, and $50\,\mu$m above the top of lattices for marker waveguides. The refractive index at the focus point of materials is slightly and permanently changed, which creates a three-dimensional effective potential for photons. The waveguides arranged in flexible arrays are shaped by moving the focus point of laser at a constant speed of 10 mm/s, which confine the single-mode light of 810 nm in the center. Laser is manipulated freely in three dimension by a high precise three-axis motion stage. Helical waveguides are fabricated by circularly shifting the transverse focus point that uniformly moves in the longitudinal trajectory. The cross-sections of examples containing triangular lattices are detailed in Supplementary Information.

The effective Hamiltonian and quasienergy of helical waveguides calculated by Floquet-Bloch theory:

The helical waveguides in triangular lattices break the translational invariant in the z direction, in which the wavefunction $\psi(x, y, z)$ of photons are described by the paraxial equation [12],

$$i\partial_z\psi(x,y,z) = -\frac{1}{2k_0}\left(\partial_x\hat{x} + \partial_y\hat{y}\right)^2\psi(x,y,z) - \frac{k_0\Delta n(x,y,z)}{n_0}\psi(x,y,z), \tag{5}$$

where $k_0 = 2\pi n_0/\lambda$ is the wave number in bulk medium with refractive index $n_0 = 1.514$, and $\Delta n(x, y, z)$ represents the distribution of refractive index that changes not only along transverse directions but also along the longitudinal z axis with a repetition period $T = 8$ mm and a rotation frequency $W = 2\pi/T$ in the fabricated waveguide lattice. By introducing a coordinate transformation $x' = x - RW\cos(Wz+\phi)$, $y' = y - RW\sin(Wz+$

$\phi)$, $z' = z$, the distribution of $\Delta n(x',\, y')$ is independent on z' and then the paraxial equation is transformed as,

$$\begin{aligned} i\partial_{z'}\psi(x',y',z') = &-\frac{1}{2k_0}\left(\partial_x\hat{x} + \partial_y\hat{y} + i\mathbf{A}(z')\right)^2\psi(x',y',z') \\ &-\left(\frac{k_0R^2W^2}{2} + \frac{k_0\Delta n(x',y')}{n_0}\right)\psi(x',y',z'), \end{aligned} \tag{6}$$

where $\mathbf{A}(z') = k_0RW[\sin(Wz'+\phi),\, -\cos(Waz'+\phi)]$ and ϕ is the initial modulation phase of helical waveguides.

Consequently, by tight-binding approximation, the evolution of photons are described by a time-dependent Hamiltonian that breaks the time-reversal symmetry as Eq. (3). To analyze the quasienergy of Floquet-Bloch states $|\Psi_\alpha(\mathbf{r},z)\rangle = e^{-i\varepsilon_\alpha z}\,|u_\alpha(\mathbf{r},z)\rangle$ with a band index α, we perform a Fourier transformation to the time-dependent Hamiltonian $\hat{H}(z)$ as [46, 47],

$$\hat{H}^F_{nm} = nW\delta_{nm} + \int_0^{2\pi/W}\hat{H}(z)e^{i(n-m)Wz}\mathrm{d}z, \tag{7}$$

where n and m are Fourier component indexes. By neglecting the influence of $|n-m| > 1$ terms, the static effective Hamiltonian that is independent on z reads [48]

$$\hat{H}^{\mathrm{Eff}} = \hat{H}^F_0 + \frac{1}{W}[\hat{H}^F_{+1},\, \hat{H}^F_{-1}], \tag{8}$$

where $\hat{H}^F_0 = \hat{H}^F_{n=0,m=0}$, $\hat{H}^F_{+1} = \hat{H}^F_{n,n-1}$ and $\hat{H}^F_{-1} = \hat{H}^F_{n,n+1}$. After diagonalizing the effective Hamiltonian $\hat{H}^{\mathrm{Eff}}$, the quasienergies ε are calculated for different parameters in Fig. 4(b).

Supporting Information

Supporting Information is available from the Wiley Online Library or from the author.

Acknowledgements

We thank Q. Wang at the Nanyang Technological University for helpful discussions. This research is supported by the National Key R&D Program of China (No. 2019YFA0308700, 2019YFA0706302, 2017YFA0303700), the National Natural Science Foundation of China (No. 11904229, 61734005, 11761141014, 11690033, 12174187, 92163216, 92150302), the Science and Technology Commission of Shanghai Municipality (STCSM) (No. 20JC1416300, 2019SHZDZX01), the Shanghai Municipal Education Commission (SMEC) (No. 2017-01-07-00-02-E00049), and China Postdoctoral Science Foundation (No. 2020M671091). X.-M.J. acknowledges additional support from a Shanghai talent program and support from Zhiyuan Innovative Research Center of Shanghai Jiao Tong University.

References

[1] D. J. Thouless, M. Kohmoto, M. P. Nightingale, M. den Nijs, *Phys. Rev. Lett.* **1982**, *49*, 6 405.

[2] D. Xiao, M.-C. Chang, Q. Niu, *Rev. Mod. Phys.* **2010**, *82*, 3 1959.

[3] C. Nayak, S. H. Simon, A. Stern, M. Freedman, S. Das Sarma, *Rev. Mod. Phys.* **2008**, *80*, 3 1083.

[4] E. Kapit, M. Hafezi, S. H. Simon, *Phys. Rev. X* **2014**, *4*, 3 031039.

[5] M. A. H. Vozmediano, M. I. Katsnelson, F. Guinea, *Physics Reports* **2010**, *496*, 4 109.

[6] M. Aidelsburger, S. Nascimbene, N. Goldman, *C. R. Phys.* **2018**, *19*, 6 394.

[7] N. Levy, S. A. Burke, K. L. Meaker, M. Panlasigui, A. Zettl, F. Guinea, A. H. C. Neto, M. F. Crommie, *Science* **2010**, *329*, 5991 544.

[8] F. Guinea, M. I. Katsnelson, A. K. Geim, *Nat. Phys.* **2010**, *6*, 1 30.

[9] J. Yuan, H. Cai, C. Wu, S.-Y. Zhu, R.-B. Liu, D.-W. Wang, *Phys. Rev. B* **2021**, *104*, 3 035410.

[10] M. Aidelsburger, M. Atala, S. Nascimbène, S. Trotzky, Y. A. Chen, I. Bloch, *Phys. Rev. Lett.* **2011**, *107*, 25 255301.

[11] K. Fang, Z. Yu, S. Fan, *Nat. Photon.* **2012**, *6*, 11 782.

[12] M. C. Rechtsman, J. M. Zeuner, Y. Plotnik, Y. Lumer, D. Podolsky, F. Dreisow, S. Nolte, M. Segev, A. Szameit, *Nature* **2013**, *496*, 7444 196.

[13] Y. Lumer, M. A. Bandres, M. Heinrich, L. J. Maczewsky, H. Herzig-Sheinfux, A. Szameit, M. Segev, *Nat. Photon.* **2019**, *13*, 5 339.

[14] P. E. Lammert, V. H. Crespi, *Phys. Rev. Lett.* **2000**, *85*, 24 5190.

[15] S. Azevedo, F. Moraes, *Phys. Lett. A* **1998**, *246*, 3 374.

[16] H. Ochoa, R. Zarzuela, Y. Tserkovnyak, *Phys. Rev. Lett.* **2017**, *118*, 2 026801.

[17] X.-Q. Sun, P. Zhu, T. L. Hughes, *Phys. Rev. Lett.* **2021**, *127*, 6 066401.

[18] Z.-K. Lin, Q. Wang, Y. Liu, H. Xue, B. Zhang, Y. Chong, J.-H. Jiang, *Nat. Rev. Phys.* **2023**, *5*, 8 483.

[19] Y. Deng, W. A. Benalcazar, Z.-G. Chen, M. Oudich, G. Ma, Y. Jing, *Phys. Rev. Lett.* **2022**, *128*, 17 174301.

[20] N. D. Mermin, *Rev. Mod. Phys.* **1979**, *51*, 3 591.

[21] M. O. Katanaev, I. V. Volovich, *Annals of Physics* **1992**, *216*, 1 1.

[22] J. Paulose, B. G.-g. Chen, V. Vitelli, *Nat. Phys.* **2015**, *11*, 2 153.

[23] Y. Ran, Y. Zhang, A. Vishwanath, *Nat. Phys.* **2009**, *5*, 4 298.

[24] Z.-K. Lin, Y. Wu, B. Jiang, Y. Liu, S.-Q. Wu, F. Li, J.-H. Jiang, *Nat. Mater.* **2022**, *21*, 4 430.

[25] T. Li, P. Zhu, W. A. Benalcazar, T. L. Hughes, *Phys. Rev. B* **2020**, *101*, 11 115115.

[26] R. Biswas Rudro, T. Son Dam, *Proc. Natl. Acad. Sci. USA* **2016**, *113*, 31 8636.

[27] L. Radzihovsky, M. Hermele, *Phys. Rev. Lett.* **2020**, *124*, 5 050402.

[28] C. W. Peterson, T. Li, W. Jiang, T. L. Hughes, G. Bahl, *Nature* **2021**, *589*, 7842 376.

[29] Y. Liu, S. Leung, F.-F. Li, Z.-K. Lin, X. Tao, Y. Poo, J.-H. Jiang, *Nature* **2021**, *589*, 7842 381.

[30] A. Rüegg, C. Lin, *Phys. Rev. Lett.* **2013**, *110*, 4 046401.

[31] A. Rüegg, S. Coh, J. E. Moore, *Phys. Rev. B* **2013**, *88*, 15 155127.

[32] V. Juričić, A. Mesaros, R.-J. Slager, J. Zaanen, *Phys. Rev. Lett.* **2012**, *108*, 10 106403.

[33] Y. Chen, Y. Yin, Z.-K. Lin, Z.-H. Zheng, Y. Liu, J. Li, J.-H. Jiang, H. Chen, *Phys. Rev. Lett.* **2022**, *129*, 15 154301.

[34] C. He, Y. Shen, A. Forbes, *Light Sci. Appl.* **2022**, *11*, 1 205.

[35] C.-C. Lu, H.-Y. Yuan, H.-Y. Zhang, W. Zhao, N.-E. Zhang, Y.-J. Zheng, S. Elshahat, Y.-C. Liu, *Chip* **2022**, *1*, 4 100025.

[36] Y. Chen, J. Gao, Z.-Q. Jiao, K. Sun, W.-G. Shen, L.-F. Qiao, H. Tang, X.-F. Lin, X.-M. Jin, *Phys. Rev. Lett.* **2018**, *121*, 23 233602.

[37] M. L. N. Chen, L. J. Jiang, W. E. I. Sha, *Phys. Rev. Appl.* **2018**, *10*, 1 014034.

Table of Contents

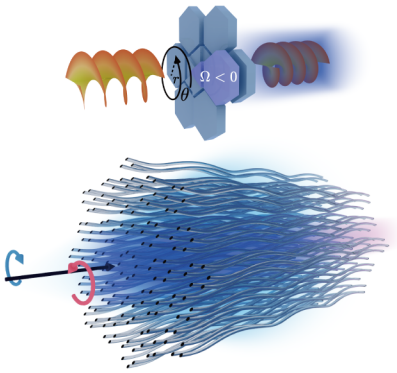

The orbital gauge field is constructed by a rotational defect on an atom-like lattice and shows a generalized and appealing perspective to control the behaviors of particles. The Hall-like transport of high-dimensional quantum states with protected orbital angular momentum represents a step towards generalized and large-scale quantum engineering.

[38] C. Sheng, Y. Wang, Y. Chang, H. Wang, Y. Lu, Y. Yang, S. Zhu, X. Jin, H. Liu, *Light Sci. Appl.* **2022**, *11*, 1 243.

[39] S. Liu, A. Vishwanath, E. Khalaf, *Phys. Rev. X* **2019**, *9*, 3 031003.

[40] Q. Wang, Y. Ge, H.-x. Sun, H. Xue, D. Jia, Y.-j. Guan, S.-q. Yuan, B. Zhang, Y. D. Chong, *Nat. Commun.* **2021**, *12*, 1 3654.

[41] L.-H. Wu, X. Hu, *Phys. Rev. Lett.* **2015**, *114*, 22 223901.

[42] H. Zhong, Y. Zhang, Y. Zhu, D. Zhang, C. Li, Y. Zhang, F. Li, M. R. Belić, M. Xiao, *Ann. Phys.* **2017**, *529*, 3 1600258.

[43] P. E. Lammert, V. H. Crespi, *Phys. Rev. B* **2004**, *69*, 3 035406.

[44] A. Cortijo, M. A. H. Vozmediano, *Nucl. Phys. B* **2007**, *763*, 3 293.

[45] W. Zhang, X. Jiang, W. Gu, J. Cheng, H. Zhou, J. Dong, D. Huang, X. Zhang, *Chip* **2023**, *2*, 2 100043.

[46] A. Gómez-León, G. Platero, *Phys. Rev. Lett.* **2013**, *110*, 20 200403.

[47] P. Titum, N. H. Lindner, M. C. Rechtsman, G. Refael, *Phys. Rev. Lett.* **2015**, *114*, 5 056801.

[48] N. Goldman, J. Dalibard, M. Aidelsburger, N. R. Cooper, *Phys. Rev. A* **2015**, *91*, 3 033632.

[49] Y.-G. Choi, et al., *Nature* **2023**, *619*, 7968 52.

[50] M. Piccardo, M. de Oliveira, A. Toma, V. Aglieri, A. Forbes, A. Ambrosio, *Nat. Photon.* **2022**, *16*, 5 359.

[51] S. Chen, Z. Xie, H. Ye, X. Wang, Z. Guo, Y. He, Y. Li, X. Yuan, D. Fan, *Light Sci. Appl.* **2021**, *10*, 1 222.

[52] X. Zeng, P. S. J. Russell, C. Wolff, M. H. Frosz, G. K. L. Wong, B. Stiller, *Sci. Adv.* **2022**, *8*, 42 eabq6064.

[53] Y.-J. Chang, et al., *Phys. Rev. Lett.* **2021**, *126*, 11 110501.

[54] S. Chen, et al., *Appl. Phys. Lett.* **2023**, *122*, 4 040503.

[55] Y. Wang, Y.-H. Lu, J. Gao, Y.-J. Chang, R.-J. Ren, Z.-Q. Jiao, Z.-Y. Zhang, X.-M. Jin, *Chip* **2022**, *1*, 1 100003.

[56] J. Gao, et al., *Chip* **2022**, *1*, 2 100007.